Nanoscale Advances

ROYAL SOCIETY OF CHEMISTRY

PAPER

View Article Online
View Journal | View Issue

Check for updates

Cite this: *Nanoscale Adv.*, 2023, **5**, 5661

A Prussian blue analog as a decorporation agent for the simultaneous removal of cesium and reactive oxygen species†

Tingyu Xue,‡[a] Fang Liu,‡[b] Bin Lu,[a] Qingrong Dong,[a] Bin Zhao,[a] Tianqing Chen,[b] Kun Zhang,[b] Jianguo Li*[c] and Jiangfeng Du *[abd]

Radioactive cesium (Cs) is a significant concern due to its role as a major byproduct of nuclear fission and its potential for radioactive contamination. Internal contamination with radioactive Cs is characterized by immoderate production of reactive oxygen species (ROS), resulting in severe radiation damage. Therefore, the development of therapeutic strategies should focus on enhancing the excretion of radioactive Cs and reducing radiation-induced oxidative damage. However, current therapeutic drugs like Prussian blue (PB) have limited efficacy in addressing these issues. In this study, we present $Cu_3[Fe(CN)_6]_2$ (CuFe) nanoparticles, a Prussian blue analog (PBA), which can not only efficiently sequester Cs but also exhibit resistance against radiation damage. The results of the adsorption studies demonstrate that CuFe outperforms PB in terms of adsorption performance. Further mechanistic investigations indicate that the increased adsorption capacity of CuFe may be attributed to the presence of additional defects resulting from the $[Fe(CN)_6]$ missing linkers. Moreover, CuFe mimics the functions of catalase (CAT) and superoxide dismutase (SOD) by effectively eliminating $O_2^{\bullet-}$ and H_2O_2 while scavenging $^{\bullet}OH$, thereby mitigating ROS induced by radiative Cs. Importantly, *in vivo* study confirms the efficient Cs decorporation capability of CuFe. The fecal cumulative excretion rate of CuFe reaches 69.5%, which is 1.45 times higher than that of PB (48.8%). These findings demonstrate that CuFe exhibits excellent Cs removal performance and ROS scavenging ability, making it an attractive candidate for the treatment of Cs contamination.

Received 6th June 2023
Accepted 11th September 2023

DOI: 10.1039/d3na00388d

rsc.li/nanoscale-advances

Open Access Article. Published on 13 September 2023. Downloaded on 2/22/2026 10:11:33 AM.
This article is licensed under a Creative Commons Attribution-NonCommercial 3.0 Unported Licence.

1 Introduction

The demand for clean energy has led to the development of nuclear energy in recent decades. However, nuclear leakage causes a significant threat to public health.[1–3] Major nuclear accidents such as Chernobyl and Fukushima released a large number of radioactive nuclides, resulting in serious mortality. Among these radioactive species, radioactive Cs (^{134}Cs and ^{137}Cs) is particularly hazardous due to its long half-life, high water solubility, and ability to migrate easily.[4–6] It can readily enter the organisms *via* ingestion or the food chain.[7] Furthermore, radioactive Cs shares chemical similarities with potassium (K), leading to its uniform distribution throughout soft tissues in organisms. Once absorbed, Cs radioactivity can trigger the production of reactive oxygen species (ROS) in cells, causing damage to biomolecules and potentially leading to tissue and organ harm as well as the development of cancer.[8,9] Therefore, efficient removal of Cs and ROS is crucial in reducing the harmful effects of Cs on human health.

To enhance the excretion rate of radioactive Cs, decorporation agents can be used. The Food and Drug Administration (FDA) has approved only one such medication, the insoluble form of bulk Prussian Blue (PB) known as ferric (III) hexacyanoferrate (II) or Radiogardase®, for the treatment of radiation contamination caused by radioactive Cs.[1,10–12] PB has a channel diameter of approximately 3.2 Å, similar to the hydration radius of Cs ion.[13] This property enables PB to selectively trap radioactive Cs in the intestines, preventing its absorption. However, the intracrystalline diffusion coefficient of Cs to bulk PB is extremely low (less than 3.3×10^{-22} m^2 s^{-1}), resulting in a slow adsorption rate of Cs.[14] To overcome this challenge, nanoscale PB and hollow PB with high specific

[a]*Department of Medical Imaging, Shanxi Key Laboratory of Intelligent Imaging and Nanomedicine, First Hospital of Shanxi Medical University, Taiyuan, 030001, Shanxi Province, China*

[b]*College of Pharmacy, Shanxi Medical University, Jinzhong, 030619, Shanxi Province, China*

[c]*National Atomic Energy Agency Nuclear Technology (Nonclinical Evaluation of Radiopharmaceuticals) Research and Development Center, CNNC Key Laboratory on Radiotoxicology and Radiopharmaceutical Preclinical Evaluation, China Institute for Radiation Protection, Taiyuan 030001, China. E-mail: ljg2547@163.com*

[d]*Collaborative Innovation Center for Molecular Imaging of Precision Medicine, Shanxi Medical University, Taiyuan 030001, Shanxi Province, China. E-mail: dujf@sxmu.edu.cn*

† Electronic supplementary information (ESI) available. See DOI: https://doi.org/10.1039/d3na00388d

‡ These authors contributed equally to this work.

© 2023 The Author(s). Published by the Royal Society of Chemistry

Open Access Article. Published on 13 September 2023. Downloaded on 2/22/2026 10:11:33 AM.
This article is licensed under a Creative Commons Attribution-NonCommercial 3.0 Unported Licence.

surface areas have been reported to exhibit improved Cs uptake kinetics.[15–20] However, further enhancement of Cs decorporation efficiency is limited by the incomplete understanding of PB's crystal engineering. Furthermore, the ROS scavenging effects of these adsorbents have not been adequately evaluated.

PB is a metal–organic framework (MOF) with catalytic and adsorption performance owing to its well-defined crystal structures, tunable pore volume and defects.[21–23] Increasing the number of defects has been proposed as a means to increase Cs adsorption sites.[24–26] Metal nodes coordinated with cyanides have also been identified as important in controlling the defect density of PB.[27–30] For example, studies have shown more vacancies in two Prussian blue analogs (PBAs), cobalt hexacyanocobaltate (CoCo) and copper hexacyanoferrate (CuFe) compared to Prussian blue,[27] and it is worth mentioning that some studies have proved that PBAs have excellent Cs adsorption properties.[31–35] However, few studies have examined the effect of metal center substitutions in PBs on Cs decorporation rates. Moreover, considering the enzyme-like characteristics of PB nanoparticles, partial substitution of transition metal elements (such as Cu and Mn) could impart PB with diverse natural enzyme-like activity, such as Mn/Cu-superoxide dismutase (Mn-SOD, Cu-SOD),[36,37] which can remove ROS and alleviate radiation damage.

In the present study, we prepared various Prussian blue analogs (PBAs) with comparable size and shape by partially replacing Fe with different transition metals. We investigated how these chemical variations impacted the adsorption properties. Subsequently, we assessed the antioxidant activity and Cs decorporation efficiency of CuFe, considering its superior adsorption selectivity, faster adsorption rate, biocompatibility, and stability. To ensure effective action in the intestines, where CuFe is needed, we developed a pH-dependent oral delivery system called Alg-CuFe, which employed alginate as a polymer to protect against stomach acid erosion. Based on our comprehensive findings, we conclude that CuFe not only enhances Cs excretion but also effectively mitigates radiation damage (Scheme 1). The development of CuFe-based strategies holds significant potential in addressing the detrimental effects of Cs on human health, which would show striking therapeutic benefits in the treatment of radioactive Cs contamination.

2 Experimental

2.1 Materials

The following materials were used without further purification: potassium ferricyanide (≥99.5%, Aladdin), manganese sulfate monohydrate (99.9%, Aladdin), ferric nitrate nonahydrate (99.99%, Aladdin), cupric acetate monohydrate (99.99, Aladdin), cobalt nitrate hexahydrate (99.99%, Aladdin), potassium ferrocyanide (99.99%, Aladdin), cesium chloride (99.9%, Aladdin), nickel tetrahydrate acetate (99.9%, Aladdin), iron(II) chloride (98%, Aladdin), citric acid (99.5%, Aladdin), DMPO (Aladdin), BMPO (DOJINDO), polyvinylpyrrolidone (TCI).

2.2 Synthesis

PB and PBA were synthesized following a previously published protocol.[38,39] The preparation of $Fe_4[Fe(CN)_6]_3$(FeFe), $Cu_3[Fe(CN)_6]_2$(CuFe), and $Ni_3[Fe(CN)_6]_2$(NiFe) is described as

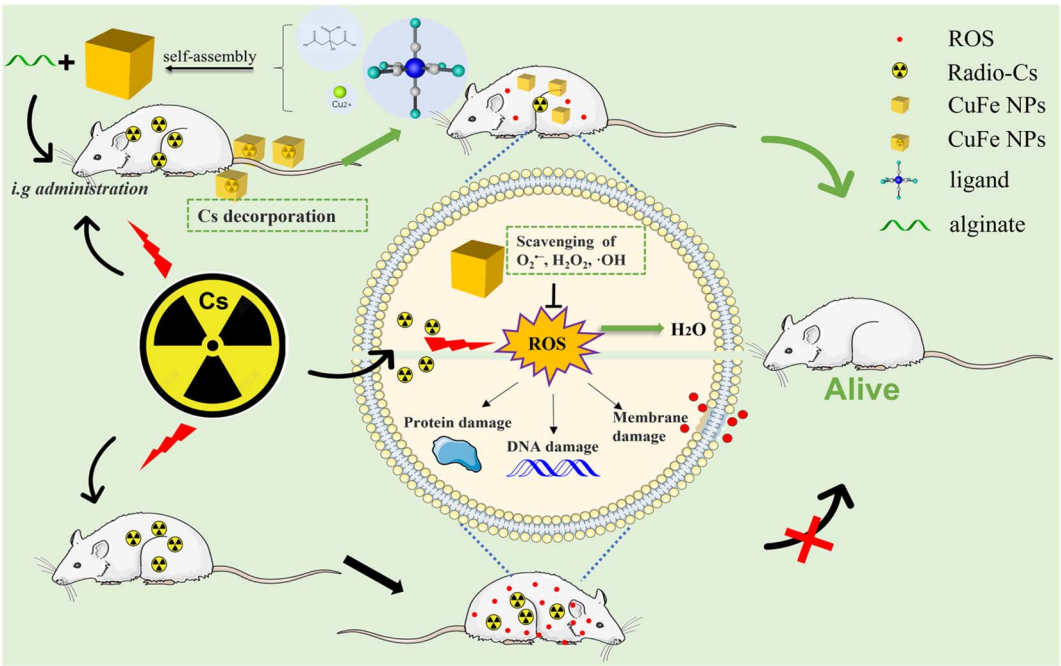

Scheme 1 Schematic illustration of the therapeutic principle based on CuFe nanoparticles for simultaneous removal of cesium and reactive oxygen species.

© 2023 The Author(s). Published by the Royal Society of Chemistry

Open Access Article. Published on 13 September 2023. Downloaded on 2/22/2026 10:11:33 AM.
This article is licensed under a Creative Commons Attribution-NonCommercial 3.0 Unported Licence.

follows: 5 mmol citric acid and 0.5–5 mmol $K_4[Fe(CN)_6]$ or $K_3[Fe(CN)_6]$ were dissolved in 20 mL of deionized water (DI) H_2O with stirring at 60 °C (solution A). In another container, 5 mmol citric acid and 2.5–7.5 mmol $Fe(NO_3)_3\cdot 9H_2O$ (or $Cu(CH_3COO)_2\cdot H_2O$, $Ni(CH_3COO)_2\cdot 4H_2O$) were dissolved in 20 mL DI H_2O (solution B). Then, solution B was added dropwise (1 mL min^{-1}) into solution A under stirring (1000 rpm) at 60 °C and stirring was continued for an additional 5 min. The reaction mixture was then cooled to room temperature under stirring (1000 rpm). The resulting mixture was centrifuged to collect the product (10 000 rpm, 10 min) and washed three times with ethanol. Finally, the obtained product was dried at 40 °C for 12 h in a vacuum oven. $Co_3[Fe(CN)_6]_2$(CoFe) and $Mn_3[Fe(CN)_6]_2$(MnFe) were synthesized by a similar procedure: CoFe was synthesized at room temperature using $Co(NO_3)_2\cdot 6H_2O$ and $K_3[Fe(CN)_6]$; MnFe was synthesized at room temperature using $MnSO_4$ and $K_3[Fe(CN)_6]$. The detailed synthesis parameters are summarized in Table S1.† Synthesis of Alg–CuFe and Alg–FeFe involved the following steps: a 4 mg mL^{-1} solution of CuFe or FeFe and 2% sodium alginate solution were mixed and stirred for 2 h to prepare Alg–CuFe and Alg–FeFe, respectively.

2.3 Characterization

Scanning electron microscopy (SEM; Hitachi S-4800) and transmission electron microscopy (TEM; Tecnai G2 spirit BioTwin) images were acquired to observe the morphology. The size distributions of the PB and PBA nanocubes were determined using a Nano particle size analyzer (DLS; Malvern Zetasizer Nano ZS90). Infrared spectroscopy (IR) was employed to obtain infrared spectra (NICOLET iS 50). X-ray diffraction (XRD) patterns were recorded using an X-ray powder diffractometer (D8 Advance). Electron paramagnetic resonance (EPR, Billerica, MA) spectra were obtained using an EPR spectrometer. The elemental composition of PB and PBAs was determined by inductively coupled plasma optical emission spectroscopy (ICP-OES; ICAP7200) and X-ray Photoelectron Spectroscopy (XPS; EXCALAB 250 XI).

2.4 Preparation of cesium standard solution

To ensure the safety of the experiment due to the radiation risk associated with the radionuclide ^{137}Cs, the stable isotope ^{133}Cs, which is non-radioactive, was used instead. Cesium chloride powder was accurately weighed and dissolved in water to prepare a 1000 mg L^{-1} cesium ion solution, which was stored at 4 °C.

2.5 *In vitro* Cs adsorption assay

In a Cs adsorption experiment, 500 μg mL^{-1} PB and PBA nanocubes were mixed with 100 ppm Cs ion solution, and then the samples were shaken at 37 °C. After 1 h, 2 h, 6 h, and 12 h, the samples were collected *via* centrifugation and filtering with a 0.22 μm filter membrane. Finally, the Cs ion concentration was measured by inductively coupled plasma-mass spectrometry (ICP-MS).

2.6 Adsorption kinetics and adsorption isotherm

Adsorption kinetics. For the adsorption kinetics study, 500 μg mL^{-1} of FeFe or CuFe nanocubes was mixed with a 100 ppm Cs ion solution. The mixture was then shaken at 37 °C. After specific time intervals of 0.1 h, 0.2 h, 1 h, 2 h, 4 h, 6 h, and 12 h, the samples were collected by centrifugation and filtered using a 0.22 μm filter membrane. Finally, the Cs ion concentration was measured by ICP-MS.

Adsorption isotherm. To investigate the adsorption isotherm, sorption isotherm experiments of CuFe and FeFe were carried out by varying the initial concentration of Cs ions from 1 ppm to 500 ppm. Then, 500 μg mL^{-1} FeFe or CuFe nanocubes was mixed with Cs ion solution, and the samples were shaken at 37 °C for 12 h. After the incubation period, the samples were filtered through a 0.22 μm filter membrane, and the concentration of cesium ions was determined using ICP-MS.

2.7 Adsorption selectivity test of CuFe

To evaluate the adsorption selectivity of CuFe for cesium ions, a solution containing Cs^+, Mg^{2+}, Zn^{2+}, Co^{2+}, Ni^{2+}, Mn^{2+} (100 ppm) and CuFe (500 μg mL^{-1}) was shaken for 24 h. Then, the sample was centrifuged and filtered through a 0.22 μm filtration membrane. The cesium ion concentration was measured by ICP-MS after 1000× dilution with deionized water.

2.8 Scavenging activity assay of H_2O_2, $O_2^{\bullet-}$ and $^{\bullet}OH$

To evaluate CuFe's ability to remove H_2O_2, the reaction was initiated by mixing CuFe with different concentrations of H_2O_2 ranging from 0.1 to 100 mM. The mixture was incubated at 30 °C for 1 minute. After the incubation period, the remaining H_2O_2 was detected by the horseradish peroxidase-3,3′,5,5′-tetramethylbenzidine (HRP-TMB) cascade reaction to determine the consumption of H_2O_2. For the scavenging activity assay of $O_2^{\bullet-}$, a total superoxide dismutase assay kit with nitro blue tetrazolium (NBT) was utilized. EPR spectroscopic measurements were also conducted to assess CuFe's scavenging capacity against ROS. EPR spectroscopic measurements: To evaluate CuFe's ability to scavenge $O_2^{\bullet-}$, a reaction mixture was prepared containing 0.1 M BMPO (spin trap), CuFe nanocubes, 1 mM xanthine, and 0.1 U mL^{-1} xanthine oxidase (XOD). Xan/XOD generates $O_2^{\bullet-}$, and CuFe nanocubes were tested for their ability to scavenge it. Two minutes after introducing XOD to initiate the production of superoxide, the ESR spectra were taken, allowing for the evaluation of CuFe's scavenging of $O_2^{\bullet-}$. To assess CuFe's scavenging capacity against hydroxyl radicals ($^{\bullet}OH$), a reaction mixture was prepared containing 0.1 M BMPO (spin trap), CuFe nanocubes, 0.02 mM Fe^{2+}, and 100 mM H_2O_2. Fe^{2+} and H_2O_2 react to produce $^{\bullet}OH$, and CuFe nanocubes were tested for their ability to scavenge $^{\bullet}OH$. Two minutes after introducing H_2O_2 to start the production of $^{\bullet}OH$, the ESR spectra were taken to evaluate CuFe's scavenging of $^{\bullet}OH$.

2.9 Cell culture

HUVEC and L02 cells were cultured in high-sugar DMEM supplemented with streptomycin (100 μg mL^{-1}), penicillin (100

Open Access Article. Published on 13 September 2023. Downloaded on 2/22/2026 10:11:33 AM.
This article is licensed under a Creative Commons Attribution-NonCommercial 3.0 Unported Licence.

units per mL), and FBS (10%). The cells were placed in a cell incubator with a controlled environment of 5% CO_2 and maintained at a temperature of 37 °C.

2.10 Cell survival assay

For cytotoxicity assays, HUVECs were seeded in 96-well plates at 5×10^3 cells per well and allowed to attach and grow. Subsequently, the culture medium was replaced with fresh medium that contained varying concentrations (ranging from 100 to 300 μg mL^{-1}) of CuFe, FeFe, or MnFe. The cells were then incubated with the respective nanocubes for an additional 24 hours. After the incubation period, the cells were washed and incubated with medium containing 10% CCK8 (Cell Counting Kit-8) for 1–1.5 h, and the absorbance was tested at 450 nm. For cell viability assays, HUVECs were similarly seeded in 96-well plates at 5×10^3 cells per well and cultured for 24 h. Then, the culture medium was replaced with fresh medium that contained 1 mM H_2O_2 and 50–100 μg mL^{-1} CuFe. After 24 h of incubation, cell viability was tested *via* a CCK-8 kit. For the antiradiation-damage assay, L02 cells were seeded in 96-well plates at 5×10^3 cells per well, cultured for 24 h and incubated with medium containing 10–20 μg mL^{-1} CuFe for 4 h. After that, the cells were irradiated with X-ray irradiation equipment at a dosage of 8 Gy. The irradiated cells were incubated for 24 h, and cell viability was tested using a CCK-8 kit.

2.11 Experimental animals

All animal experimental procedures were approved by the Ethics Committee of the China Institute for Radiation Protection (SYXK(JIN)2019-0002). The 7–8 weeks old female BALB/c normal mice were purchased from Chang-zhou Cavens Laboratory Animal Co., Ltd (China). The mice were housed at 25 °C with 50% air humidity in metabolic cages with 12 h light/dark cycles. For *in vivo* experiments, the mice were divided into three groups ($n = 6$): control group, FeFe group and CuFe group. The urine and feces were collected at 1 h, 2 h, 4 h, 6 h, 12 h, 24 h, 48 h, 72 h, and 96 h. After 96 h, the mice were sacrificed and the heart, liver, spleen, lung, kidney, muscle, and blood were gathered. The content of Cs in urine, feces, organs and blood samples was used for quantification analysis by ICP-MS. 3 mL HNO_3 and 1 mL HCl were add to each sample in a conical flask and sealed for predigestion overnight, then the flasks were placed onto a hot plate while maintaining the temperature at 150 °C until the digestion was complete. The surplus solution in each flask was diluted with 2% HNO_3 and filtered with a 220 nm filter membrane.

2.12 Hematoxylin-eosin (H&E) staining

The heart, liver, spleen, lung, kidney, stomach and intestine of mice were collected and fixed with 4% paraformaldehyde solution. After fixation, the tissues were processed for paraffin embedding. Thin slices of the embedded tissues were then prepared and stained with hematoxylin and eosin (H&E) staining.

3 Results and discussion

3.1 Formulation and characterization of the PB and PBA NPs

The hydrothermal method was employed to synthesize five types of PB and PBA NPs with similar sizes and morphologies. As illustrated in Fig. 1a, C≡N ligands were utilized to form cyanide-bridged cubic networks by combining with Fe(III, II) ions, resulting in $Fe_4[Fe(CN)_6]_3$ for PB NPs. Similarly, PBAs ($M_3[Fe(CN)_6]_2$) were obtained by partially substituting Fe with other transition metals. The coordination of different metal atoms with C or N atoms in the C≡N bridges is denoted as M_1-N≡C-M_2, simplifying the nomenclature of PB and PBA NPs as M_1M_2.

The cubic shape of all PB and PBA NPs was confirmed through TEM and SEM images. The size distribution analysis indicated that the NPs ranged from 90 nm to 200 nm (Fig. 1b, c, S1 and S2†), which was consistent with the data obtained by dynamic light scattering (DLS) measurements (Fig. S3†). The X-ray powder diffraction (XRD) patterns of PB and PBA NPs demonstrated that the peaks of all samples were compatible with the standard patterns of face-center- cubic PB NPs (JCPDS No. 73-0687), and no other impurities were detected (Fig. 1d and S4†).[33,40] As shown in Fig. 1e and S5,† the peaks of IR spectra of PB and PBA NPs at the 2000–2200 cm^{-1} range correspond to the ν(M_1-C≡N-M_2) mode. The other two characteristic peaks in the 490–600 cm^{-1} range were assigned to the Fe–C≡N and C≡N-M_2 vibration absorption peaks.[33] Inductively coupled plasma emission spectrometry (ICP-OES) analysis confirmed the presence of different transition metals in the NPs, indicating the successful incorporation of these metals (Table S2†). Overall, the PB and PBA nanoparticles were successfully synthesized with similar sizes and framework structures.

3.2 *In vitro* Cs adsorption

The adsorptive property of PB and PBAs was assessed and compared. The results of the Cs ion uptake experiments indicated that all PBAs exhibited higher adsorption efficiency compared to PB, particularly CuFe and MnFe (Fig. S7†). Based on CuFe's biocompatibility and stability (Fig. 3d and S10†), further investigations were conducted to assess its adsorption kinetics and isotherms. As depicted in Fig. 1f, CuFe could reach equilibrium with large capacity within 6 h, whereas the PB NPs required more than 12 h. Adsorption isotherm experiments were conducted to determine CuFe's adsorptive capacity using initial Cs^+ concentrations ranging from 0.5 to 500 ppm. As demonstrated in Fig. 1g, CuFe exhibited a higher maximum sorption capacity compared to FeFe (108.28 mg g^{-1} *versus* 87.32 mg g^{-1}). The faster kinetics and larger sorption capacity of CuFe may have come from more defects compared to PB. Moreover, CuFe demonstrated superior Cs adsorption selectivity. As shown in Fig. 1 h, CuFe showed no adsorption for Cu(II), Mn(II), Co(II), Zn(II) and Fe(II), only displaying minor adsorption of K(I) and Na(I). Together, these indicate that CuFe exhibits better adsorption activity and selectivity toward Cs by means of partial substitution of metal centers in PB.

© 2023 The Author(s). Published by the Royal Society of Chemistry

Open Access Article. Published on 13 September 2023. Downloaded on 2/22/2026 10:11:33 AM.
This article is licensed under a Creative Commons Attribution-NonCommercial 3.0 Unported Licence.

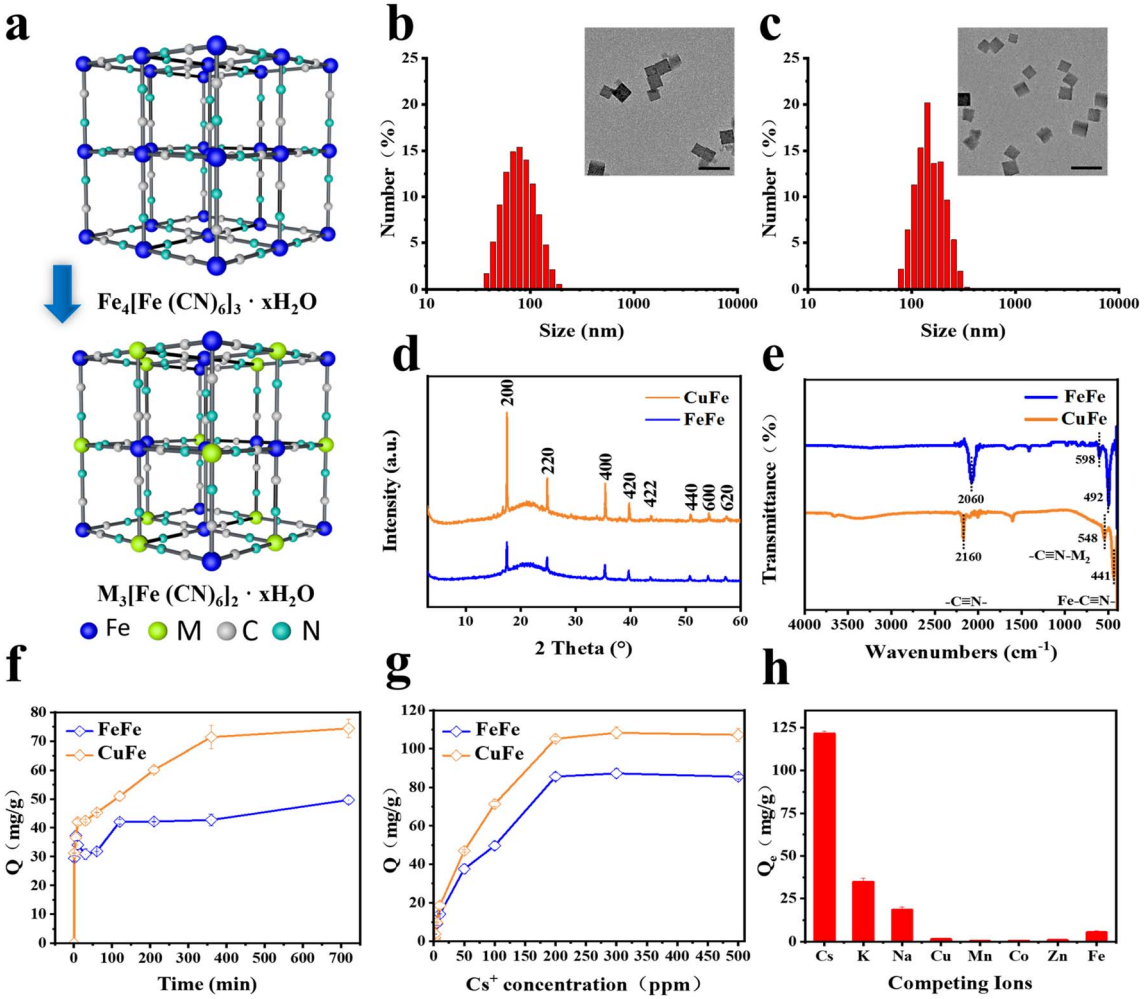

Fig. 1 (a and b) Schematic PB/PBA structures consisting of 3D regular lattice spaces surrounded by Fe(II)–CN–Fe(III) bonds (a) or M(II)–CN–Fe(III) bonds. (b and c) Size and morphology of FeFe (b) and CuFe (c) characterized by DLS and TEM (inset), scale bars: 200 nm. (d) XRD spectra of FeFe and CuFe. (e) IR spectra of FeFe and CuFe. (f) Adsorption kinetics of CuFe and FeFe using 100 ppm Cs^+ solution at pH = 7.4, T = 310.15 K, m V^{-1} = 500 μg ml^{-1} (g), adsorption isotherm of CuFe and FeFe using 0.5–500 ppm Cs + solution at pH = 7.4, T = 310.15 K, m V^{-1} = 500 μg mL^{-1} (h), adsorption selectivity test in the presence of K(I), Na(I), Cu(II), Mn(II), Co(II), Zn(II), Fe(II) (I = 100 ppm, T = 310.15 K, m V^{-1} = 500 μg mL^{-1}).

To investigate the adsorption mechanism of Cs, several characterization techniques were employed, including TEM mapping, electron paramagnetic resonance (EPR) and X-ray photoelectron spectroscopy (XPS), to analyze the crystal architectural difference between CuFe and FeFe. TEM mapping analysis of CuFe and Cs–CuFe revealed that Cs ions were adsorbed and uniformly distributed within the CuFe crystal, as depicted in Fig. 2b. As mentioned earlier, CuFe may possess more defect sites, which can contribute to its faster uptake and higher sorption capacity (Fig. 2a). Point defects or structural defects might lead to unpaired electrons, and EPR is a technique commonly used to study chemical species with unpaired electrons.[41] Therefore, EPR measurements were performed to assess the presence of defects in FeFe and CuFe. Fig. 2c shows that CuFe exhibited characteristic paramagnetic peaks, with a greater signal strength compared to FeFe. This suggests that CuFe contained more defect sites than FeFe. Finally, to further determine the structure of the defect sites, the component was determined by XPS. XPS surface analysis was used to determine the chemical components well as the ratio of Fe (II)/Fe(III), Fe/Cu, Cu/N, Fe(III)/N and C/N (Table S4†). The Fe 2p, Cu 2p, N 1s and C 1s spectra demonstrated the presence of metal and nonmetal components in the corresponding PB and PBA (Fig. 2d–h and S6†). The ratio of Fe (II)/Fe(III) in FeFe is 0.74, which was higher than the ratio of Fe/Cu (0.6) in CuFe. Moreover, the ratio of Fe(III)/N in FeFe (0.7) is smaller than the ratio of Cu/N in CuFe (3.02). These findings suggest that CuFe can form more CN and $[Fe(CN)_6]$ vacancies. More $[Fe(CN)_6]$ missing linkers in CuFe lead to the presence of additional adsorption sites.[25] Consequently, CuFe exhibits enhanced adsorption characteristics due to the increased number of available adsorption sites.

3.3 Antioxidant and radiation protection assay

Once radioactive Cs is taken up by cells, ionizing radiation in the nucleus and cytoplasm can induce the generation of reactive oxygen species (ROS). Intracellular antioxidant enzymes are often unable to quickly remove excessive ROS, and radiation

Open Access Article. Published on 13 September 2023. Downloaded on 2/22/2026 10:11:33 AM.
This article is licensed under a Creative Commons Attribution-NonCommercial 3.0 Unported Licence.

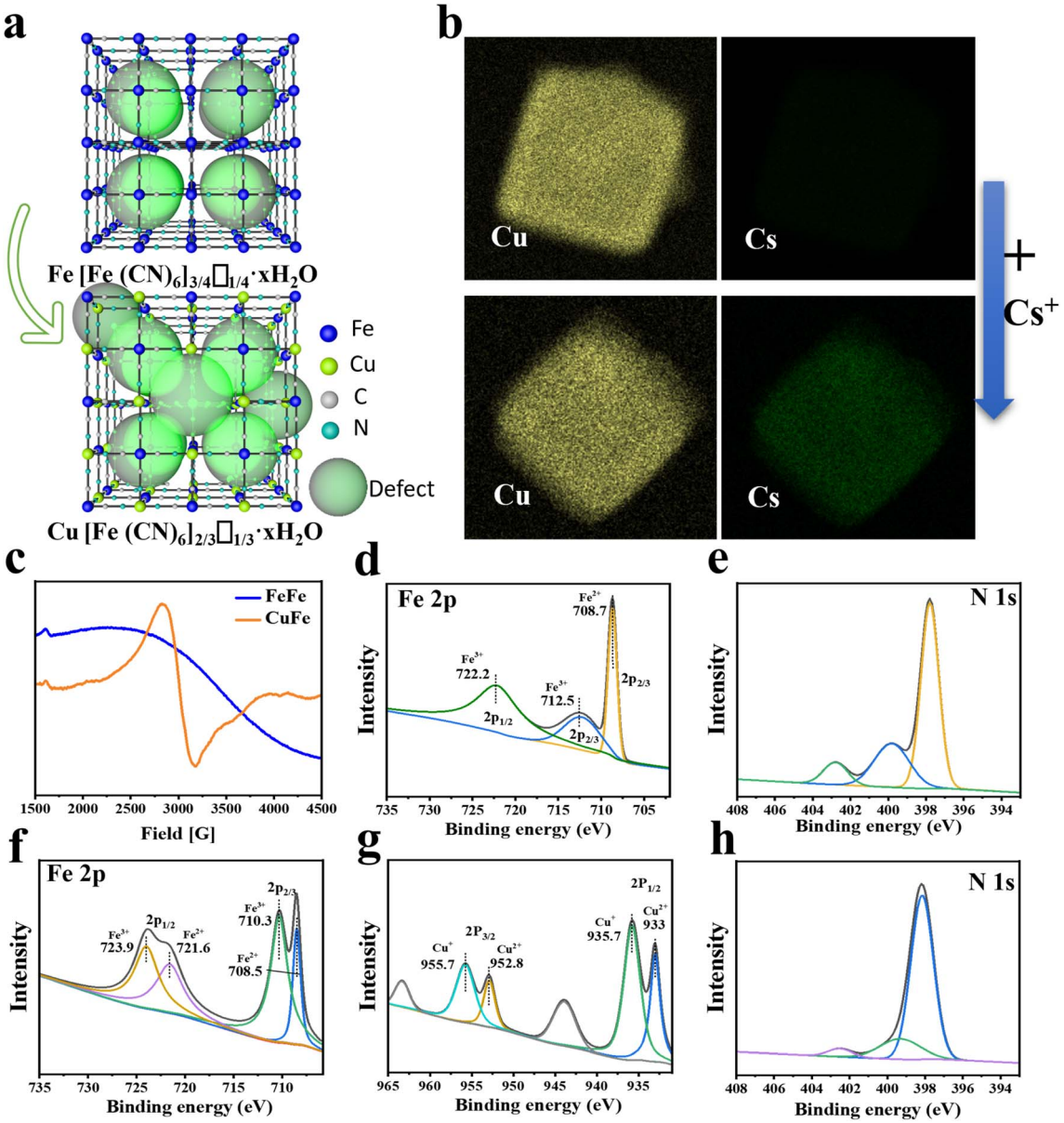

Fig. 2 (a) Schematic illustration of the defect in FeFe and CuFe. One-quarter of the [Fe(CN)$_6$] linker is missing, generating defects (green spheres) in FeFe, and one-third of the [Fe(CN)] linker is missing in CuFe. (b) TEM mapping of CuFe before and after the uptake of the Cs ion. (c) EPR spectra of FeFe and CuFe. (d and e), Fe 2p (d) and N 1s (e) XPS spectra of FeFe. (f–h) Fe 2p (f), Cu 2p (g) and N 1 s (h) XPS spectra of CuFe.

can also lead to the inactivation of enzymes. Therefore, the elimination of ROS is crucial in preventing oxidative damage.[42–45]

PBA has been reported to possess nano-enzyme properties,[46] and thus the antioxidant activity of CuFe was evaluated. The CAT-like activities of CuFe were first assessed by measuring the decomposition rate of H_2O_2. In Fig. 3a, it can be found that the catalytic capacity of CuFe was intensified with the increase of H_2O_2 concentration. The K_m and V_{max} value of CuFe with H_2O_2 as the substrate was 71.03428 μM and 57.50567 μM s^{-1} respectively, indicating favorable CAT-like activities of CuFe for the degradation of H_2O_2. To test the superoxide dismutase (SOD)-like activity of CuFe, electron spin resonance (ESR) spectroscopy was employed. As shown in Fig. 3b, the EPR signal of $O_2^{\bullet-}$ in the CuFe group decreased significantly compared with the control group, indicating the efficient $O_2^{\bullet-}$ scavenging ability. Besides, the SOD-like activities were then further investigated using the total superoxide dismutase assay kit with NBT (Fig. 3c). In the presence of CuFe, the signal of NBT (which can be reduced by $O_2^{\bullet-}$) was clearly inhibited. With an increase in CuFe concentration, the scavenging capability improved, indicating outstanding SOD-like activity of CuFe. Furthermore, the scavenging activity of $^{\bullet}OH$ was also assessed using EPR spectroscopy. Fig. 3d demonstrates that the signal strength decreased in the presence of CuFe, indicating successful scavenging of $^{\bullet}OH$. The scavenging activity increased with higher CuFe concentrations. Overall, these findings indicate that CuFe could effectively eliminate ROS, suggesting its potential to

© 2023 The Author(s). Published by the Royal Society of Chemistry

Open Access Article. Published on 13 September 2023. Downloaded on 2/22/2026 10:11:33 AM.
This article is licensed under a Creative Commons Attribution-NonCommercial 3.0 Unported Licence.

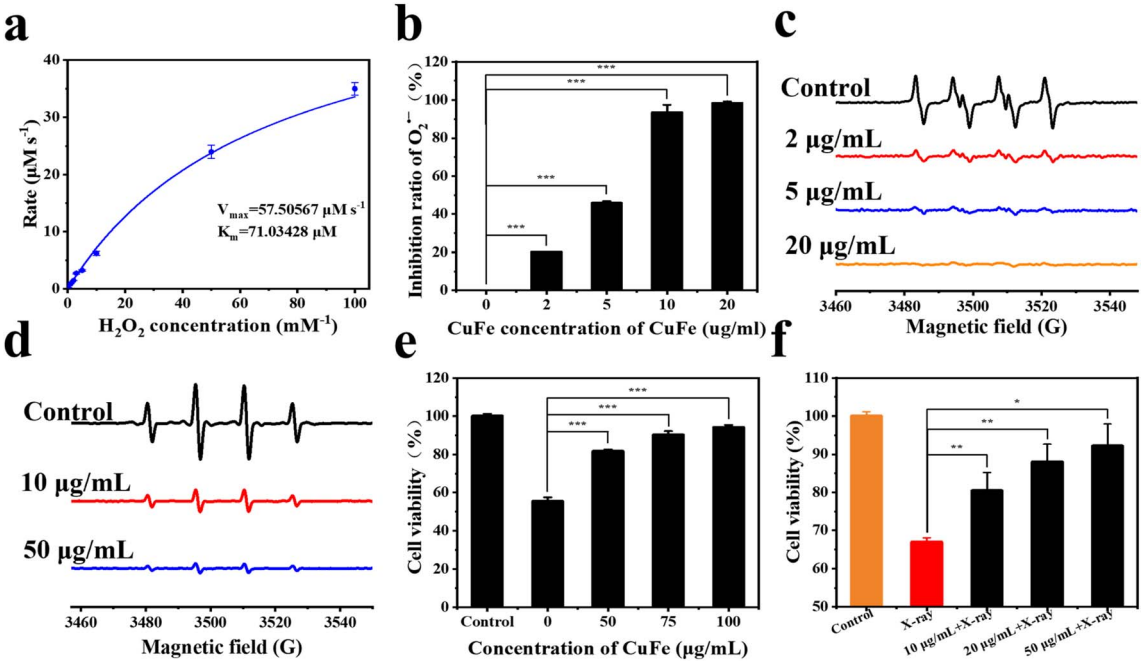

Fig. 3 Multiple anti-oxidative activities of CuFe. (a) CAT-like activity of CuFe. Steady-state kinetic assay of CuFe with H_2O_2. V_{max} is the maximal reaction velocity, and k_m is the Michaelis–Menten constant. (b and c) SOD-like activity of CuFe. Inhibition ratio of $O_2^{\bullet-}$ using a total superoxide dismutase assay kit with NBT without and with 0–20 μg mL^{-1} CuFe (b). ESR spectra of $O_2^{\bullet-}$ in the Xan/XOD generating system without (control) and with 0–20 μg mL^{-1} CuFe (c). (d) $^{\bullet}$OH-scavenging activity. ESR spectra of $^{\bullet}$OH in the Fe^{2+}/H_2O_2 generating system without (control) and with 10–50 μg mL^{-1} CuFe. (e and f) L02 cell survival assays in the presence of H_2O_2 (1 mM) (e) and X-rays (f) without (control) and with CuFe.

alleviate the negative effects of oxidative stress damage. CuFe's CAT-like activity, SOD-like activity, and $^{\bullet}$OH scavenging activity contribute to its antioxidant properties, which may help counteract oxidative damage induced by ionizing radiation and contribute to cellular protection.

Then, the cytotoxicity of CuFe was investigated using HUVECs. Cell viability was measured using CCK-8 assays. The results, as shown in Fig. S8,† confirmed the negligible cytotoxicity of CuFe when the concentration ranged from 0 to 300 mg mL^{-1}. Moreover, CuFe also exhibited no cytotoxicity towards normal liver cells (L02) (Fig. S8†), indicating the good biosafety of CuFe.

Inspired by the ROS-scavenging activities and biosecurity of CuFe, the intracellular antioxidative performance of CuFe was further investigated in the presence of H_2O_2 and radiation. Compared with the control group, treatment with 1 mM H_2O_2 for 24 h resulted in significant cellular toxicity. However, with the assistance of CuFe, cell viability increased by approximately 25–40% (Fig. 3e). Additionally, the intracellular ROS level was assessed using DCFH-DA as the fluorescence probe (Fig. S9†). The fluorescence intensity decreased significantly in the presence of CuFe compared to the control group, indicating the efficient ROS scavenging effect of CuFe. Furthermore, the survival rate of cells can be increased under X-ray irradiation after introducing CuFe (Fig. 3f). These results collectively demonstrate that CuFe not only effectively eliminates ROS but also reduces oxidative stress injury, thereby protecting cells against the damaging effects of ionizing radiation.

3.4 *In vivo* Cs decorporation

In order to evaluate the decorporation ability of CuFe for Cs *in vivo*, a series of experiments were conducted. Prior to the *in vivo* experiment, we used simulated gastric fluid (SGF) and phosphate-buffered saline (PBS) to simulate the gastrointestinal environment and to assess the stability and adsorption performance of Alg–CuFe. In SGF, alginates formed crosslinks with each other and encapsulated the nanoparticles, as depicted in Fig. S10.† Additionally, when Alg–CuFe was transferred from SGF to PBS, there was minimal loss in the Cs sequestration ability of CuFe (Fig. 4a and b). Moreover, almost no copper ions were released during this period. The potential risk of excessive exposure to copper ions was eliminated (Fig. S11†). These experiments demonstrated the feasibility of pH-dependent oral delivery systems. Subsequently, an *in vivo* experiment was performed to verify the Cs decorporation of Alg–CuFe. Mice were randomly divided into the control group, FeFe group and CuFe group. Both Cs and Alg-CuFe were administered through intragastric administration. All the mice were contaminated with 100 μg kg^{-1} of Cs^+ using ^{133}CsCl solution. After five minutes, 20 μg kg^{-1} Alg–CuFe was administered. Urine and feces were collected from the mice at different time points (1 h–96 h). After 96 hours, the heart, liver, spleen, lung, kidney and muscle were collected. The Cs^+ content of urine, feces and organs was analyzed using ICP-MS to measure the amount of excretion and deposition of Cs ions.

The results of the *in vivo* experiment regarding the cumulative excretion rate of cesium and the final Cs content in the

Open Access Article. Published on 13 September 2023. Downloaded on 2/22/2026 10:11:33 AM.
This article is licensed under a Creative Commons Attribution-NonCommercial 3.0 Unported Licence.

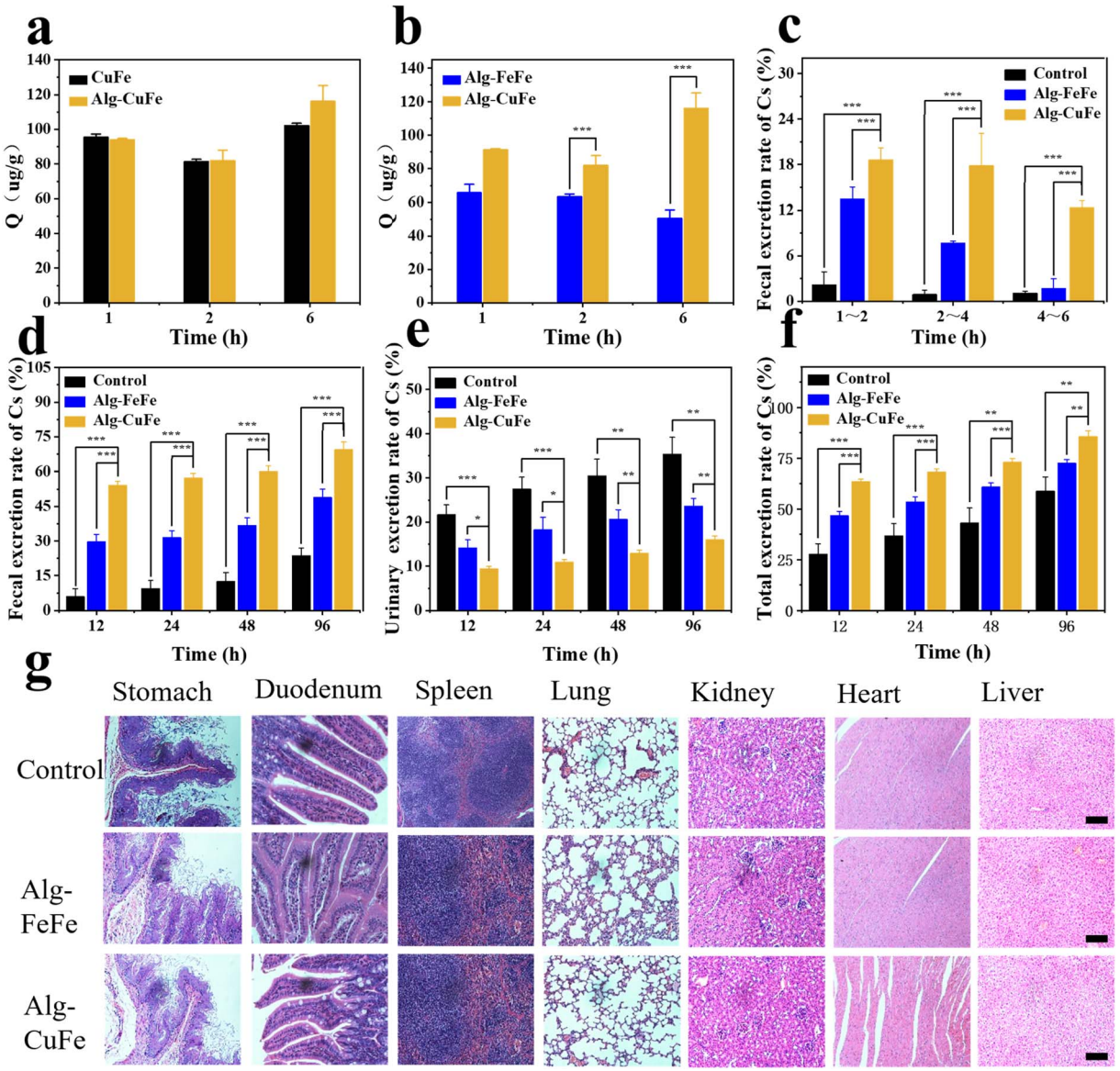

Fig. 4 (a) Cesium adsorption assays of CuFe and Alg–CuFe after transferring from simulated gastric fluid to PBS; (b) cesium adsorption assays of Alg–FeFe and Alg–CuFe after transferring from simulated gastric fluid to PBS. (c and d) Excretion rate of Cs ions in feces compared to the initial Cs dose. (e) Excretion rate of Cs ions in urine compared to the initial Cs dose. (f) Total excretion rate of Cs ions compared to the initial Cs dose. (g) Photomicrographs of heart, liver, spleen, lung, kidney, stomach and duodenum with H&E staining. Scale bars, 200 μm.

organs are presented in Fig. 4 and Fig. S12.† In comparison to the control and FeFe groups, the CuFe group exhibited a higher excretion of Cs through feces (Fig. 4c–f and S12a–e†), confirming the adsorption effect of CuFe in the intestinal tract. CuFe facilitated rapid fecal excretion of Cs, particularly within 1–2 h, 2–4 h and 4–6 h time intervals (18.6%, 17.8% and 12.3% respectively), whereas the FeFe group showed lower fecal excretion rates of only 13.4%, 7.6%, and 1.69% during the corresponding time intervals (Fig. 4c). Furthermore, the cumulative fecal excretion and total excretion rates were higher in the CuFe group compared to the FeFe group, as depicted in Fig. 4d, f, S12a and e.† Additionally, the Cs content in the heart, liver, spleen, lung, kidney, and muscles of the CuFe-treated group were 26.2 ng g^{-1}, 12.52 ng g^{-1}, 20.4 ng g^{-1}, 20.4 ng g^{-1}, 39.65 ng g^{-1}, and 45.59 ng g^{-1}, respectively, which were lower than the corresponding values in the FeFe-treated group (Fig. S12f†). These findings provide strong evidence for the excellent decorporation performance of CuFe. Finally, H&E staining was employed to assess the biosafety of Alg–CuFe. Organs from different groups were collected at the end of treatment. As shown in Fig. 4g, there were no significant histopathological changes under the microscope, which ruled out the gastric, intestinal and other major organ toxicities of Alg–CuFe. In conclusion, these results demonstrate that CuFe showed outstanding Cs sequestration performance, which could promote the excretion of Cs and prevent the Cs from being reabsorbed in the intestinal tract.

© 2023 The Author(s). Published by the Royal Society of Chemistry

Open Access Article. Published on 13 September 2023. Downloaded on 2/22/2026 10:11:33 AM. This article is licensed under a Creative Commons Attribution-NonCommercial 3.0 Unported Licence.

4 Conclusions

In conclusion, this study introduces a nanoantidote for radioactive cesium that exhibits high efficiency in decorporation and mitigating radiation damage. The *in vitro* adsorption experiments demonstrated that the cesium adsorption performance of PB and PBA depends on the chemical composition, with PBAs exhibiting significantly higher adsorption efficiency than PB. The presence of more defect sites in CuFe was identified as a crucial factor contributing to its enhanced cesium adsorption capacity. CuFe also exhibited low cytotoxicity and selective adsorption of cesium, making it a decorporation drug candidate. *In vivo* tests confirmed that CuFe outperformed PB in terms of decorporation efficacy, effectively preventing cesium deposition in tissues and organs. Moreover, CuFe demonstrated strong ROS scavenging ability, offering potential protection against radiation damage caused by the radionuclide cesium. This study opens up a new possibility for the development of decorporation drugs targeting radioactive cesium contamination.

Author contributions

Conceptualization, Jiangfeng Du, Jianguo Li; synthesis of nanostructured and nanoscale materials, Tingyu Xue, Qingrong Dong, Kun Zhang; properties of nanoscale materials, Tingyu Xue, Bin Lu, Bin Zhao, Tingqing Chen; *in vivo*/*in vitro* experiments, Tingyu Xue, Fang Liu; data curation, Tingyu Xue, Fang Liu, Bin Lu; writing – original draft preparation, Tingyu Xue, Bin Lu; writing – review and editing, Jiangfeng Du, Bin Lu; funding acquisition Jiangfeng Du, all authors have read and agreed to the published version of the manuscript.

Conflicts of interest

The authors declare that they have no known competing financial interests or personal relationships that could influence the work reported in this paper.

Acknowledgements

This work was supported by the Four "Batches" Innovation Project of Invigorating Medical through Science and Technology of Shanxi Province (2023XM036). We really appreciate for the support of the Key Technology of Radiopharmaceutical Safety Evaluation for Nuclear Energy Development Program, Scientific Research Program for Young Talents of China National Nuclear Corporation, and State Key Laboratory of Radiation Medicine and Protection.

Notes and references

1 J. Estelrich and M. A. Busquets, *Int. J. Mol. Sci.*, 2021, **22**, 780.
2 J. Qian, S. Cai, S. Yang and D. Hua, *J. Mater. Chem. A*, 2017, **5**, 22380–22388.
3 C. Shi, X. Wang, Q. Sun, L. Chen, J. Guan, L. He, Y. Zhang, Y. Xu, J. Cao, Z. Chai, S. Wang and J. Diwu, *Environ. Sci.: Nano*, 2022, **9**, 2704–2712.
4 J. H. Kim, H. Anwer, Y. S. Kim and J. W. Park, *Chemosphere*, 2021, **280**, 130419.
5 N. Dehbashi Nia, S.-W. Lee, S. Bae, T.-H. Kim and Y. Hwang, *Appl. Surf. Sci.*, 2022, **590**, 153101.
6 Y. Yoshizawa, *Nucl. Phys.*, 1958, **5**, 122–140.
7 H. Rai and M. Kawabata, *Front. Plant Sci.*, 2020, **11**, 528.
8 J. G. Kiang and A. O. Olabisi, *Cell Biosci.*, 2019, **9**, 25.
9 E. Cho, J. Kim, C. W. Park, K. W. Lee and T. S. Lee, *J. Hazard. Mater.*, 2018, **360**, 243–249.
10 M. Altagracia-Martinez, J. Kravzov, N. Martínez, C. Ríos and N. López, *Orphan Drugs: Res. Rev.*, 2012, **2**, 13–21.
11 D. R. Melo, J. L. Lipsztein, R. Leggett, L. Bertelli and R. Guilmette, *Health Phys.*, 2014, **106**, 592–597.
12 P. Sinharoy, S. S. Meena, D. Banerjee, G. Sugilal and C. P. Kaushik, *BARC Newsl.*, 2022, 82–84.
13 G.-R. Chen, Y.-R. Chang, X. Liu, T. Kawamoto, H. Tanaka, A. Kitajima, D. Parajuli, M. Takasaki, K. Yoshino, M.-L. Chen, Y.-K. Lo, Z. Lei and D.-J. Lee, *Sep. Purif. Technol.*, 2015, **143**, 146–151.
14 H. Fujita, H. Sasano, R. Miyajima and A. Sakoda, *Adsorption*, 2014, **20**, 905–915.
15 C. Lavaud, M. Kajdan, E. Compte, J.-C. Maurel, J. Lai Kee Him, P. Bron, E. Oliviero, J. Long, J. Larionova and Y. Guari, *New J. Chem.*, 2017, **41**, 2887–2890.
16 J. Qian, J. Xu, L. Kuang and D. Hua, *Chempluschem*, 2017, **82**, 888–895.
17 H. S. Bambra and M. Mazhar, *Int. J. Trend Sci. Res. Dev.*, 2019, **3**, 874–877.
18 N. L. Torad, M. Hu, M. Imura, M. Naito and Y. Yamauchi, *J. Mater. Chem.*, 2012, **22**, 18261–18267.
19 F. Carniato, G. Gatti, C. Vittoni, A. M. Katsev, M. Guidotti, C. Evangelisti and C. Bisio, *Molecules*, 2020, **25**, 3447.
20 I. Lee, S. H. Kim, M. Rethinasabapathy, Y. Haldorai, G. W. Lee, S. R. Choe, S. C. Jang, S. M. Kang, Y. K. Han, C. Roh, W. S. Cho and Y. S. Huh, *Sci. Rep.*, 2018, **8**, 4540.
21 H. L. B. Bostrom, I. E. Collings, D. Daisenberger, C. J. Ridley, N. P. Funnell and A. B. Cairns, *J. Am. Chem. Soc.*, 2021, **143**, 3544–3554.
22 Z. Y. Yu, Y. Duan, J. D. Liu, Y. Chen, X. K. Liu, W. Liu, T. Ma, Y. Li, X. S. Zheng, T. Yao, M. R. Gao, J. F. Zhu, B. J. Ye and S. H. Yu, *Nat. Commun.*, 2019, **10**, 2799.
23 S. Wang, X. Ge, C. Lv, C. Hu, H. Guan, J. Wu, Z. Wang, X. Yang, Y. Shi, J. Song, Z. Zhang, A. Watanabe and J. Cai, *Nanoscale*, 2020, **12**, 9557–9568.
24 N. Ruankaew, N. Yoshida, Y. Watanabe, A. Nakayama, H. Nakano and S. Phongphanphanee, *Phys. Chem. Chem. Phys.*, 2019, **21**, 22569–22576.
25 M. Ishizaki, S. Akiba, A. Ohtani, Y. Hoshi, K. Ono, M. Matsuba, T. Togashi, K. Kananizuka, M. Sakamoto, A. Takahashi, T. Kawamoto, H. Tanaka, M. Watanabe, M. Arisaka, T. Nankawa and M. Kurihara, *Dalton Trans.*, 2013, **42**, 16049–16055.
26 J. H. Lee and S. Y. Kwak, *ACS Omega*, 2022, **7**, 3222–3229.

© 2023 The Author(s). Published by the Royal Society of Chemistry

Open Access Article. Published on 13 September 2023. Downloaded on 2/22/2026 10:11:33 AM.
This article is licensed under a Creative Commons Attribution-NonCommercial 3.0 Unported Licence.

27 A. Takahashi, H. Tanaka, D. Parajuli, T. Nakamura, K. Minami, Y. Sugiyama, Y. Hakuta, S. Ohkoshi and T. Kawamoto, *J. Am. Chem. Soc.*, 2016, **138**, 6376–6379.
28 S. S. Kaye and J. R. Long, *Catal. Today*, 2007, **120**, 311–316.
29 A. Simonov, T. De Baerdemaeker, H. L. B. Bostrom, M. L. Rios Gomez, H. J. Gray, D. Chernyshov, A. Bosak, H. B. Burgi and A. L. Goodwin, *Nature*, 2020, **578**, 256–260.
30 D. Wang, I. W. He, J. Liu, D. Jana, Y. Wu, X. Zhang, C. Qian, Y. Guo, X. Chen, A. K. Bindra and Y. Zhao, *Angew. Chem., Int. Ed.*, 2021, **60**, 26254–26259.
31 S. Ayrault, B. Jimenez, E. Garnier, M. Fedoroff, D. J. Jones and C. Loos-Neskovic, *J. Solid State Chem.*, 1998, **141**, 475–485.
32 P. A. Haas, *Sep. Sci. Technol.*, 1993, **28**, 2479–2506.
33 H. Hayashi, *Phys. Chem. Chem. Phys.*, 2022, **24**, 9374–9383.
34 C. Loos-Neskovic, S. Ayrault, V. Badillo, B. Jimenez, E. Garnier, M. Fedoroff, D. J. Jones and B. Merinov, *J. Solid State Chem.*, 2004, **177**, 1817–1828.
35 P. Nielsen, B. Dresow and H. C. Heinrich, *Z. Naturforsch., B: J. Chem. Sci.*, 1987, **42**, 1451–1460.
36 D. Chao, Q. Dong, Z. Yu, D. Qi, M. Li, L. Xu, L. Liu, Y. Fang and S. Dong, *J. Am. Chem. Soc.*, 2022, **144**, 23438–23447.
37 T. Wu, S. Huang, H. Yang, N. Ye, L. Tong, G. Chen, Q. Zhou and G. Ouyang, *ACS Mater. Lett.*, 2022, **4**, 751–757.
38 J. Chen, Q. Wang, L. Huang, H. Zhang, K. Rong, H. Zhang and S. Dong, *Nano Res.*, 2018, **11**, 4905–4913.
39 Q. Jia, F. Su, Z. Li, X. Huang, L. He, M. Wang, Z. Zhang, S. Fang and N. Zhou, *ACS Appl. Bio Mater.*, 2019, **2**, 2143–2154.
40 L. Cao, Y. Liu, B. Zhang and L. Lu, *ACS Appl. Mater. Interfaces*, 2010, **2**, 2339–2346.
41 X. Cheng, X. Huo, B. Yang, W. Li, Q. Wang and Y. Zhang, *J. Cleaner Prod.*, 2022, **334**, 130220.
42 Y. Miao, J. Sheng, X. Wang, C. Shi, Q. Sun, T. Liu and J. Diwu, *New J. Chem.*, 2021, **45**, 9518–9525.
43 C. Shi, X. Wang, J. Wan, D. Zhang, X. Yi, Z. Bai, K. Yang, J. Diwu, Z. Chai and S. Wang, *Bioconjugate Chem.*, 2018, **29**, 3896–3905.
44 S. Das, C. J. Neal, J. Ortiz and S. Seal, *Nanoscale*, 2018, **10**, 21069–21075.
45 X. Ren, M. Huo, M. Wang, H. Lin, X. Zhang, J. Yin, Y. Chen and H. Chen, *ACS Nano*, 2019, **13**, 6438–6454.
46 R. Zhou, P. Wang, Y. Guo, X. Dai, S. Xiao, Z. Fang, R. Speight, E. W. Thompson, P. J. Cullen and K. Ostrikov, *Nanoscale*, 2019, **11**, 19497–19505.

© 2023 The Author(s). Published by the Royal Society of Chemistry